Hindawi
Complexity
Volume 2020, Article ID 8360361, 17 pages
https://doi.org/10.1155/2020/8360361

Research Article

High-Resolution Remote-Sensing Image-Change Detection Based on Morphological Attribute Profiles and Decision Fusion

Chao Wang,[1,2,3] Hui Liu,[4] Yi Shen,[1] Kaiguang Zhao,[3] Hongyan Xing ,[1] and Haotian Wu[1]

[1]*Key Laboratory of Meteorological Disaster, Ministry of Education (KLME)/Collaborative Innovation Center on Forecast and Evaluation of Meteorological Disasters (CIC-FEMD)/Joint International Research Laboratory of Climate and Environment Change (ILCEC), Nanjing University of Information Science and Technology, Nanjing 210044, China*
[2]*Jiangxi Province Key Laboratory of Water Information Cooperative Sensing and Intelligent Processing Nanchang Institute of Technology, Nanchang 330099, China*
[3]*College of Food, Agricultural, and Environmental Sciences, The Ohio State University, Wooster 44691, USA*
[4]*College of Computer and Information Engineering, Hohai University, Nanjing 211100, China*

Correspondence should be addressed to Hongyan Xing; xinghy@nuist.edu.cn

Received 29 March 2019; Revised 17 October 2019; Accepted 14 February 2020; Published 23 March 2020

Academic Editor: Marcio Eisencraft

Change detection (CD) is essential for accurate understanding of land surface changes with multitemporal Earth observation data. Due to the great advantages in spatial information modeling, Morphological Attribute Profiles (MAPs) are becoming increasingly popular for improving the recognition ability in CD applications. However, most of the MAPs-based CD methods are implemented by setting the scale parameters of Attribute Profiles (APs) manually and ignoring the uncertainty of change information from different sources. To address these issues, a novel method for CD in high-resolution remote sensing (HRRS) images based on morphological attribute profiles and decision fusion is proposed in this study. By establishing the objective function based on the minimum of average interscale correlation, a morphological attribute profile with adaptive scale parameters (ASP-MAPs) is presented to exploit the spatial structure information. On this basis, a multifeature decision fusion framework based on the Dempster–Shafer (D-S) theory is constructed for obtaining the CD map. Experiments of multitemporal HRRS images from different sensors have shown that the proposed method outperforms the other advanced comparison CD methods, and the overall accuracy (OA) can reach more than 83.9%.

1. Introduction

With the development of remote sensing system, change detection (CD) has attracted widespread interest as one of the most important applications in remote sensing [1]. The accurate processing and understanding of the changes of land covers is a significant issue in different applications pertaining human activities, such as dynamic monitoring of land use, vegetation health, and environment [2–4]. The wild use of the new generation of high-resolution sensors (e.g., IKONOS, QuickBird, and GF2) has further broadened the applications of CD technology [5]. Compared with medium- and low-resolution remote sensing images, a greater amount of spatial and thematic information of land covers is contained in high-resolution remote sensing (HRRS) images, which makes it feasible to recognize different types of complex structures within a scene [6]. However, due to that, an object with a variety of shapes is composed by many pixels and the spectral information is very limited, these properties of HRRS images make the traditional pixel-based CD methods which are based on spectral differences ineffective [7].

In order to address this issue, numerous studies have focused on importing spatial structure information as a supplement [8, 9]. It has been proved that such information is highly effective to improve the recognition ability of CD in HRRS images [10]. In the current literature, supervised machine learning methods are most widely used for feature

extraction in CD applications [11, 12]. However, these methods require a large number of labeled examples to identify model parameters and avoid overfitting [13]. Meanwhile, a variety of unsupervised spatial structure information extraction methods for CD in HRRS images have been proposed. Different strategies, such as object-based methods combined with image segmentation [14], linear transformation-based methods [15], Markov Random Field-(MRF-) based methods [16], multiscale analysis methods [17], and a number of indicators as the change intensity measurement [18–20], have been employed in these studies. In recent years, in order to deal with a high level of details due to the increased resolution of HRRS images that are not significant or even disadvantageous for CD, the Morphological Attribute Profiles (MAPs) have been introduced into CD applications [7, 21].

Among the most effective methods of spatial modeling for the analysis of HRRS images, the operators in MAPs can be efficiently implemented based on the multiscale representation of land covers via tree structures [22, 23]. Compared with traditional feature extraction strategies based on the given filter windows, the MAPs can expand the analysis unit to all connected pixels with similar attribute, which is helpful to accurately extract the spatial structure information of the object that the pixel belongs to. Moreover, their effectiveness has been proved in decreasing the complexity of image and extracting spatial structure information in CD applications [24]. Even so, there are still several issues in most MAPs-based CD methods [25, 26]: (1) In order to highlight the representative spatial structure information while reducing the reductant information in a limited number of Attribute Profiles (APs), a reasonable set of scale parameters should be adaptively determined. However, the theory of MAPs does not give explicit criteria and the scale parameters are currently determined manually by experience. (2) In view of the complexity of land cover changes within a scene, when combining multiple change information for APs and other features, few studies take the uncertainty of change information from different sources into consideration.

Concerning the above challenges, a novel method for CD in HRRS images based on morphological attribute profiles and decision fusion is proposed, and the contributions of this study can be summarized as follows:

(1) A morphological attribute profile with adaptive scale parameters (ASP-MAPs) is presented to extract representative APs while reducing redundant information. By establishing the objective function based on the minimum of average interscale correlation, the scale parameter set for each attribute can be adaptively determined through iterative computations.

(2) In addition, a multifeature decision fusion framework based on Dempster–Shafer (D-S) theory [27] is constructed. In this framework, change intensity indicator (CII) and confidence indicator of evidence (CIE) are presented to describe the change information and the corresponding belief degree, respectively, and the decision fusion strategy has been proved efficiently to improve the reliability of decisions through reducing the uncertainty of change information from different sources.

The rest of this paper is organized as follows: Section 2 briefly introduces the MAPs theory and the adopted attributes; in Section 3, the detailed implementation process of the proposed method is demonstrated; Section 4 contains an analysis and discussion of the experiments; the conclusion is drawn in Section 5.

2. MAPs Theory and the Adopted Attributes

2.1. MAPs Theory. MAPs theory is developed from set theory, in which the connected region corresponding to a pixel is extracted though spectral similarity and spatial connectivity as the basic analysis unit, and then, multiscale operators are designed with different attributes. The calculation process of MAPs is briefly introduced as follows [28]: let B denote a gray image, i denote a pixel in B, and k denote a gray level. Then, a binary image $\mathrm{Th}_k^i(B)$ can be obtained:

$$\mathrm{Th}_k^i(B) = \begin{cases} 1, & B(i) > k, \\ 0, & \text{otherwise.} \end{cases} \tag{1}$$

Traverse all pixels in B to get a series $\mathrm{Th}_k(B)$ and set $\Gamma^i(B) = \max(k)$ as the result of the opening operation of i. On this basis, by using the symmetry of attribute transformation, the closing operation $\Phi^i(B) = \min(k)$ of i can be obtained. Let $T_w \in \{T_1, T_2, \ldots, T_W\}$ denote the wth scale parameter, W denote the total number of scales, and the opening profile $\Psi(\Gamma(B))$ and closing profile $\Psi(\Phi(B))$ are represented as follows:

$$\begin{cases} \Psi(\Gamma(B)) = \left(\Gamma_{T_w}(B)\right), & \forall w \in \{0, \ldots, W\}, \\ \Psi(\Phi(B)) = \left(\Phi_{T_w}(B)\right), & \forall w \in \{0, \ldots, W\}. \end{cases} \tag{2}$$

By combining $\Psi(\Gamma(B))$ and $\Psi(\Phi(B))$, the MAPs can be obtained.

2.2. Adopted Attributes. Based on the research outcomes related to MAPs, four attributes have proved to be effective in HRRS image classification and CD applications are adopted in this study, including Area, Diagonal, Standard Deviation, and Normalized Moment of Inertia (NMI) [25, 28].

For the connected region corresponding to pixel i, Area reflects the area size; Diagonal describes the diagonal length of the minimum external rectangle attribute; Standard Deviation describes the degree of gray variation; and NMI reflects the shape and gravity position.

3. Method

Based on the image registration and radiation normalization of multitemporal HRRS images, the implement of the

proposed method mainly includes ASP-MAPs construction, change information description based on CII, and multifeature decision fusion. A specific description of the implementation process is shown in Figure 1.

3.1. ASP-MAPs Construction. As shown in Figure 1, during the process of ASP-MAPs construction, the scale parameters are firstly determined by the following objectives: a limited number of APs with different scale parameters should highlight the representative spatial structure features of typical land covers within a scene, thus improving the recognition ability of the changes that happen in these land covers; besides, reducing the redundant information between APs also requires a reasonable scale parameter set [29, 30]. On this basis, it is expected that the smaller the average interscale correlation of APs is, the more representative the APs are. Based on this principle, the specific process of ASP-MAPs construction is as follows.

3.1.1. Gradient Similarity (GRSIM). In order to measure the interscale correlations of APs, an appropriate similarity measurement is needed. According to the theory of MAPs, the pixels that conform to the attribute range determined by the corresponding scale parameter have the greatest response, which are presented as newly generated edges (or objects). Therefore, the similarity measurement should be sensitive to the edge changes. Based on the above analysis, a gradient vector-based similarity measurement, GRSIM, is presented: The third-order Sobel filter [31] is used to extract the gradient information and define the GRSIM index between images $B1$ and $B2$ as follows:

$$\mathrm{GRSIM}_{B1,B2} = \frac{4\sigma_{Z1}\sigma_{Z2}\sigma_{M1,M2}}{\sigma_{M1}\sigma_{M2}\left(\sigma_{Z1}^2 + \sigma_{Z2}^2\right)}, \tag{3}$$

where $\mathbf{Z}1$ and $\mathbf{Z}2$ denote the gradient amplitude matrix of $B1$ and $B2$, respectively; $\mathbf{M}1$ and $\mathbf{M}2$, respectively, denote the gradient direction matrix of $B1$ and $B2$; σ_{Z1}, σ_{Z2}, σ_{M1}, σ_{M2}, σ_{Z1}^2, σ_{Z2}^2, and $\sigma_{M1,M2}$ denote the standard deviation, variance, and covariance, respectively. The greater the value of $\mathrm{GRSIM}_{B1,B2}$ is, the higher the correlation between $B1$ and $B2$ will be.

3.1.2. Adaptive Scale Parameter Extraction Based on GRSIM. The steps of the adaptive scale parameter extraction strategy are as follows:

Step 1: set the interval $[T_{\min}, T_{\max}]$ and the number of scales W for each attribute to adaptively search the optimal scale parameter set. According to suggestions in [8, 28, 32], set Area interval as [500, 28000], Diagonal interval as [10, 100], Standard Deviation interval as [10, 70], NMI interval as [0.2, 0.5], and W as no more than 10. In addition, according to the results of the following multiple experiments, it is suggested to set W as 6 in this study.

Step 2: in order to avoid trapping in the local optimum, the wth ($w \in \{1, 2, \ldots, W\}$) scale parameter should be located within the interval Sub_w. Set Sub_w as in the following equation:

$$\mathrm{Sub}_w = \left[T_{\min} + \frac{(w-1)\left(T_{\max} - T_{\min}\right)}{W}, T_{\min} + \frac{w\left(T_{\max} - T_{\min}\right)}{W}\right]. \tag{4}$$

Step 3: define objective function as follows:

$$\mathrm{GRSIM}_{\mathrm{sum}} = \sum_{w=1}^{W-1} \mathrm{GRSIM}_{w,w+1}, \tag{5}$$

where $\mathrm{GRSIM}_{w,w+1}$ denotes the GRSIM of two adjacent APs. According to equations (3)–(5), iteratively compute the $\mathrm{GRSIM}_{\mathrm{sum}}$ with all combinations of scale parameters and regard the combination corresponding to the minimum of $\mathrm{GRSIM}_{\mathrm{sum}}$ as the extracted optimal scale parameter set. On this basis, the ASP-MAPs of multitemporal images can be obtained according to equation (2) in Section 2.1.

3.2. Change Information Description Based on CII. In order to uniformly describe the change information extracted from both ASP-MAPs and original spectra, a change intensity indicator, CII, is calculated as follows:

Step 1: extract the difference image between different temporal APs of the same scale parameter by difference disposal, and the difference image set based on ASP-MAPs for each attribute can be obtained.

Step 2: extract the difference image between different temporal images of the same band by difference disposal, and the difference image set based on the original spectra can be obtained.

Step 3: in the difference image, since the gray value of pixel i reflects the possibility of whether i is a changed pixel, it is given a normalized treatment in the interval of $[0, 255]$ as one of CIIs corresponding to i. Computing the CIIs based on ASP-MAPs and all bands in original images, then five CII sets based on Area, Diagonal, Standard deviation, NMI, and original spectra corresponding to i can be obtained.

3.3. Multifeature Decision Fusion. D-S theory is a decision theory of multisource evidence fusion, and one significant advantage of D-S theory is the strong ability in explicit estimations of uncertainty of multisource evidences [26, 33]. Therefore, a decision fusion framework is constructed in this study for fusing change information from ASP-MAPs and original spectra.

3.3.1. Basic Probability Assignment Formula (BPAF). According to D-S theory, denote A as a nonempty subset of 2^Θ, Θ as a hypothesis space, and the BPAF of A as $m(A)$. The BPAF m: $2^\Theta \longrightarrow [0, 1]$ should satisfy the following constraints:

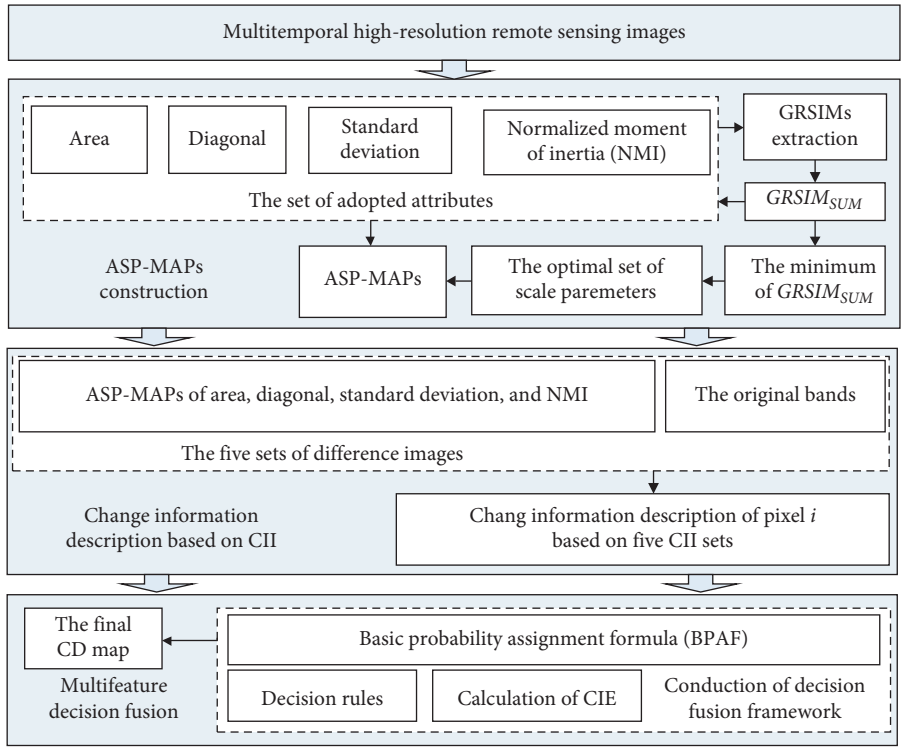

Figure 1: Flowchart of the proposed method.

$$\begin{cases} m(\varnothing) = 0, \\ \sum_{A \in 2^{\Theta}} m(A) = 1, \end{cases} \tag{6}$$

where $m(A)$ represents the belief degree of A, and the computation of $m(A)$ is shown as follows:

$$m(A) = \frac{\left[\sum_{F_1 \cap F_2 \ldots \cap F_N = A} \left(\prod_{1 \le n \le N} m_n(F_n)\right)\right]}{\left[\sum_{F_1 \cap F_2 \ldots \cap F_N \ne \varnothing} \left(\prod_{1 \le n \le N} m_n(F_n)\right)\right]}, \tag{7}$$

where N denotes the total number of evidences, $m_n(F_n)$ denotes the BPAF computed from the *nth* evidence $F_n \in 2^{\Theta}$, and $F_n \ne \varnothing$.

3.3.2. Calculation of CIE. In order to measure the belief degree of CIIs from different sources (including Area, Diagonal, Standard deviation, NMI, and the original spectra), a confidence indicator of evidence, CIE, is presented. For each evidence, the CIE can be calculated with equation (8). For each CII, the bigger CIE means that the higher relief degree should be given in the decision fusion process:

$$\mathrm{CIE} = \frac{\left[\sum_{w=1}^{W-1}\left(\sum_{w'=w+1}^{W}\left(1/\left(1 + \mathrm{GRSIM}_{w,w'}\right)\right)\right)\right]}{[0.5W(W-1)]}. \tag{8}$$

3.3.3. Construction of Decision Fusion Framework. Define the decision fusion framework as Θ: {CT, NT}, where CT and NT represent the changed and unchanged pixel, respectively. Thus, the nonempty subsets include {CT}, {NT}, and {CT, NT}. For each pixel i, the BPAF can be established through the following equations:

$$\begin{aligned} m_n(\{\mathrm{CT}\}) &= \mathrm{CII}_n \times \mathrm{CIE}_n, \\ m_n(\{\mathrm{NT}\}) &= (1 - CII_n)\mathrm{CIE}_n, \\ m_n(\{\mathrm{CT}, \mathrm{NT}\}) &= 1 - \mathrm{CIE}_n, \end{aligned} \tag{9}$$

where CII_n and CIE_n represent the *nth* CII and CIE corresponding to pixel i. On this basis, calculate $m(\{\mathrm{CT}\})$, $m(\{\mathrm{NT}\})$, and $m(\{\mathrm{CT}, \mathrm{NT}\})$ for pixel i through equation (7), and the decision rules are shown as follows:

$$\begin{cases} m(\{\mathrm{CT}\}) > m(\{\mathrm{NT}\}), \\ m(\{\mathrm{CT}\}) > m(\{\mathrm{CT}, \mathrm{NT}\}). \end{cases} \tag{10}$$

If i satisfies the above rules, i is recognized as a changed pixel; else, i is recognized as an unchanged pixel. Finally, the CD map can be obtained by traversing all pixels based on the above decision procedure.

4. Experiment and Analysis

In the experiments, three datasets of multitemporal HRRS images were used. By combining quantitative evaluation and visual inspection, the performance of the proposed method was verified by comparison with a variety of advanced CD methods.

4.1. Dataset Description. Dataset 1 was a set of aerial remote sensing images with red, green, and blue bands of Nanjing, China; the acquisition times were March 2009 and February

2012, respectively; the spatial resolution was 0.5 m, and the image size was 512 × 512 pixels, as shown in Figure 2(a). Dataset 2 was a set of QuickBird images with red, green, and blue bands of Chongqing, China; the acquisition times were September 2007 and August 2011, respectively; the spatial resolution was 2.4 m, and the image size was 512 × 512 pixels, as shown in Figure 2(b). Dataset 3 was a set of SPOT-5 pan-sharpened images with red, green, and blue bands of Shanghai, China; the acquisition times were June 2004 and July 2008, respectively; the spatial resolution was 2.5 m, and the image size was 512 × 512 pixels, as shown in Figure 2(c). Besides, a number of representative areas marked in red boxes (patches I1, I3, and I5) and blue boxes (patches I2, I4, and I6) in Figure 2 were chosen for detailed comparison and analysis.

The reasons for selecting these three datasets for the experiments were as follows: these datasets represented different urban scenes and were mainly composed of buildings, roads, vegetation, wasteland, etc., which were helpful to verify the ability of the proposed method in recognizing the changes happened on these typical land covers; moreover, using these datasets was beneficial to evaluate the applicability and stability of the proposed method in CD applications.

4.2. Experimental Setup. In order to evaluate the performance of the proposed method synthetically, five advanced CD methods were adopted for comparison experiments: the improved change vector analysis (CVA) methods, including CVA-Expectation Maximum (CVA-EM) method (Method 1) [3], spectral angle mapper-based method (Method 2) [7], and spectral and texture features-based method (Method 3) [34]; the MAPs-based method (Method 4) [8]; and the Deep Learning- (DL-) based method (Method 5) [13]. The implementation steps and parameter settings of comparison methods were consistent with the original references, and the adaptively extracted scale parameter sets of the proposed method are reported in Tables 1–3.

4.3. General Results and Analysis of Datasets. The CD maps and the reference maps of three datasets are shown in Figures 3–5, in which white pixels represent changed pixels and black pixels represent unchanged pixels. In addition, the reference maps were manually delineated by field investigation and visual interpretation.

The quantitative evaluation results of the different methods are reported in Tables 4–6. In all three datasets, the overall accuracy (OA) of the proposed method reached more than 83.9%, and the fluctuation range was less than 1.5%, which were significantly better than that of the comparison methods. Therefore, among the challenges brought by the different data sources, the proposed method possessed advantages of high accuracy and stability.

Among three CVA-based CD methods, Methods 1 and 2 only used spectral difference as the basis of CD and had weak ability in identifying false changes that were produced by insignificant detail changes; hence, the false positive (FP) rate and false negative (FN) rates were over 30% and 20%, respectively. Since the texture difference was introduced as a supplement, the three evaluation indicators showed an obvious improvement in Method 3. Therefore, it was necessary to handle the information of a pixel considering its spatial neighborhood system in order to generate more accurate CD maps. However, in Method 3, a series of specified filter windows were defined manually to extract the texture features, which made it hard to be in consistent with the inherent shape and area of the corresponding object the current pixel belongs to. By contrast, the MAPs could extract more accurate spatial structure information based on unfixed local regions constituted of all connected pixels with similar attribute.

Compared with the proposed method, although Method 4 adopted APs to extract the change information, the results of OA were significantly lower and fluctuated by more than 8% in all three datasets in this study. These may be mainly due to that in Method 4, the scale parameters were set manually, which neglected to highlight the representative spatial structure information while reducing reductant information in APs; and the final CD map was obtained by a single threshold based on the change information from different sources with the same weight, which ignored uncertainty of change information. Based on this analysis, additional experiments and discussion about the impact on OA with adaptive scale parameter extraction and decision fusion are presented in Section 4.5.

As one of the DL-based methods, Method 5 utilized the dense skip connections within the UNet++ architecture to learn multiscale feature maps from different semantic levels. It had shown outstanding performance in terms of CD based on the satellite image pair set which was presented by Lebedev [35], and the OA could reach more than 89%. However, Method 5 showed low accuracy and bad stability in all three datasets in this study. It was expected that the lack of training samples was the primary reason why there was a huge difference of OA among different datasets. Therefore, DP-based methods could not be implemented or obtain reliable results in CD applications without sufficient training samples. However, it is certain that with the increase of training samples, the performance of Method 5 would be significantly improved.

4.4. Visual Inspection of Representative Patches. The results of the representative patches in each dataset are reported in Figure 6 (patches I1 and I2), Figure 7 (patches I3 and I4), and Figure 8 (patches I5 and I6). The CD maps for each representative patch were discussed as follows.

As shown in Figures 6–8, the proposed method showed better performance than the other comparison methods in most patches, especially for the changes happened in typical urban land covers such as buildings, roads, uncultivated lands, and vegetations, which were mainly embodied in the following: in the yellow rectangle of I1, only Methods 1, 3, and 4 and the proposed method almost extracted the complete contour of the new gymnasium; for the area severely affected by the shadows as shown in the purple rectangle of I1, a large number of false positives existed in all

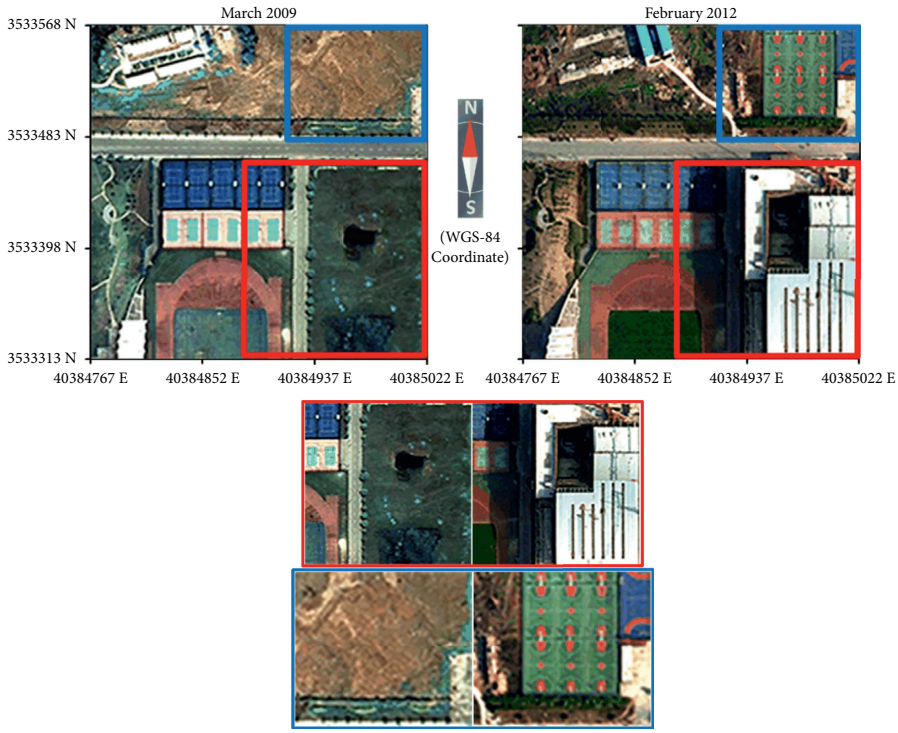

(a)

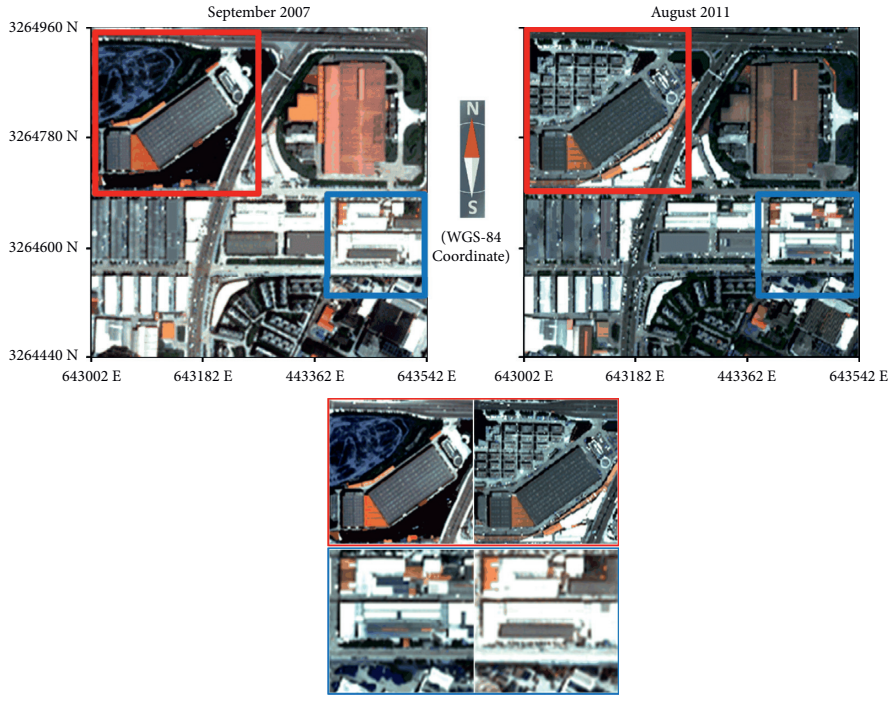

(b)

Figure 2: Continued.

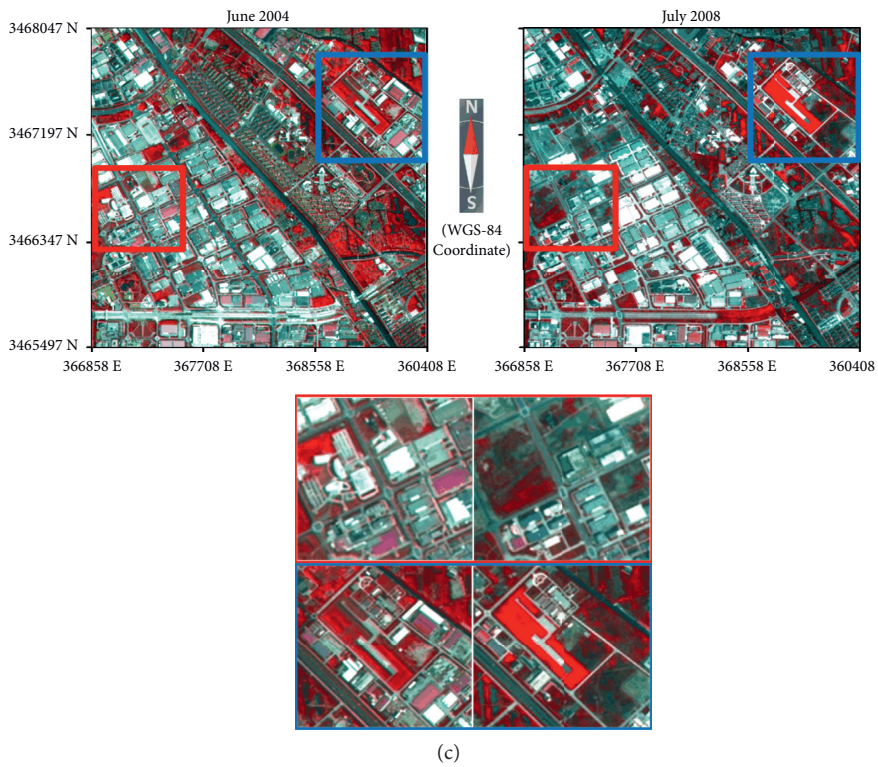

Figure 2: Experimental datasets: (a) Dataset 1 and patches I1 (red box) and I2 (blue box); (b) Dataset 2 and patches I3 (red box) and I4 (blue box); (c) Dataset 3 and patches I5 (red box) and I6 (blue box).

Table 1: Extracted scale parameter set of dataset 1.

Attribute	Scale parameter set of dataset 1
Area	{3722, 7724, 12851, 16992, 20134, 23768}
Diagonal	{12.4, 29.2, 48.3, 62.4, 81.4, 89.3}
Standard deviation	{18, 25, 34, 42, 54, 67}
NMI	{0.23, 0.28, 0.32, 0.38, 0.44, 0.48}

Table 2: Extracted scale parameter set of dataset 2.

Attribute	Scale parameter set of dataset 2
Area	{1264, 7127, 9958, 15724, 20217, 22125}
Diagonal	{15.7, 31.2, 48.6, 68.1, 79.3, 92.2}
Standard deviation	{14, 26, 33, 45, 56, 62}
NMI	{0.22, 0.26, 0.33, 0.37, 0.43, 0.49}

Table 3: Extracted scale parameter set of dataset 3.

Attribute	Scale parameter set of dataset 3
Area	{902, 5421, 12467, 16894, 20789, 21986}
Diagonal	{14.6, 33.2, 51.3, 59.2, 79.3, 89.6}
Standard deviation	{16, 23, 34, 46, 52, 66}
NMI	{0.21, 0.28, 0.31, 0.39, 0.44, 0.46}

five comparison methods except the proposed method; in the yellow rectangle of I2, the new basketball court was missed by Methods 1 and 2, the new tennis court was missed by Method 4; in the purple rectangle of I2, the new alley was extracted only by Methods 1 and 4 and the proposed method; for the new cluster of buildings as shown in the yellow rectangle of I3, the CD effects of Methods 3 and 4 and the proposed method were obviously better than the other comparison methods; in terms of the new artificial targets with significant spectral difference as shown in the purple rectangle of I3, only Method 5 showed a number of false positives; in the yellow rectangle of I4, only Methods 1 and 3 and the proposed method extracted the new buildings, while there were fewest false positives in the proposed method; in the purple rectangle of I4, the changes of border trees in the purple rectangle of I4 were only accurately recognized by the proposed method; in both yellow and purple rectangles of I5 and I6, there were large areas constituted with uncultivated lands and vegetations produced by the demolition of building clusters, and the proposed method and Method 4 showed better performance in presenting the change details of individual buildings; for the unchanged areas with significant spectral difference as shown in the green rectangle of I6, a large number of false positives existed in Methods 1 and 2.

Therefore, experiments of multitemporal HRRS images from different sensors showed that the proposed method outperformed the other comparison methods in both quantitative evaluation and visual inspection.

4.5. Efficiency Analysis of Adaptive Scale Parameters and Decision Fusion. In order to verify the effectiveness of the proposed adaptive scale parameter extraction strategy and decision fusion framework, respectively, the following two

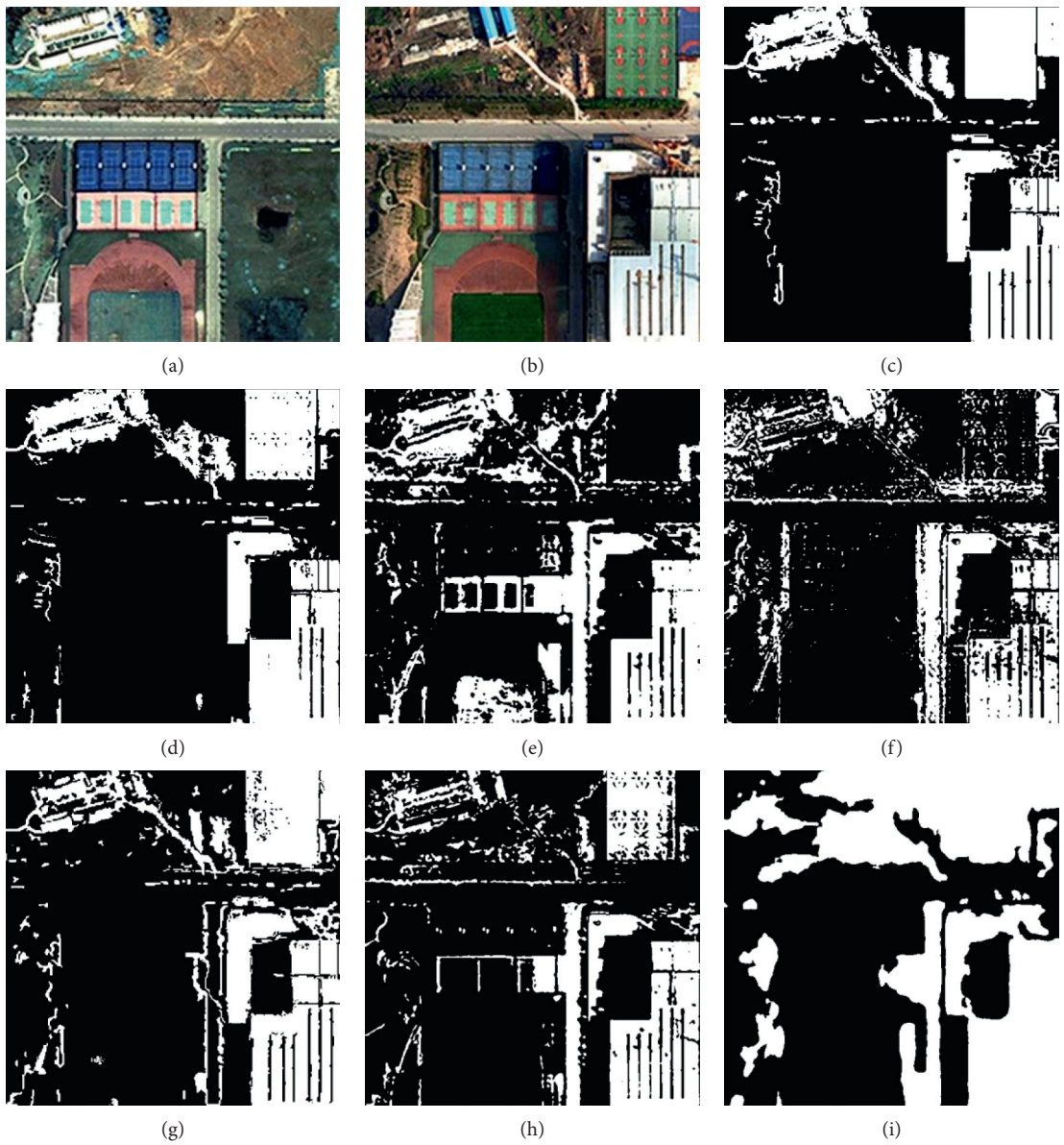

(a) (b) (c)

(d) (e) (f)

(g) (h) (i)

Figure 3: CD maps of dataset 1: (a-b) dataset 1; (c) reference map of dataset 1; (d–i) CD maps obtained in dataset 1 using the proposed method and Methods 1, 2, 3, 4, and 5, respectively.

(a) (b) (c)

Figure 4: Continued.

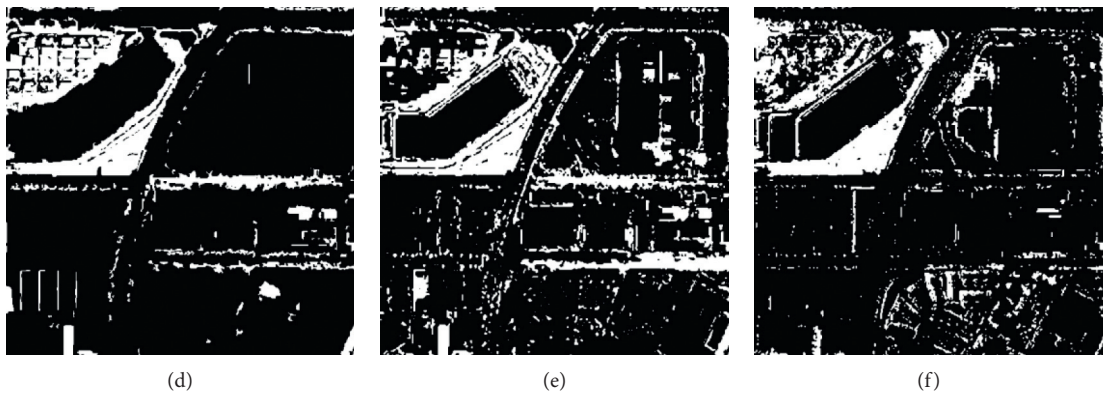

(d) (e) (f)

(g) (h) (i)

Figure 4: CD maps of dataset 2: (a-b) dataset 2; (c) reference map of dataset 2; (d–i) CD maps obtained in dataset 2 using the proposed method and Methods 1, 2, 3, 4, and 5, respectively.

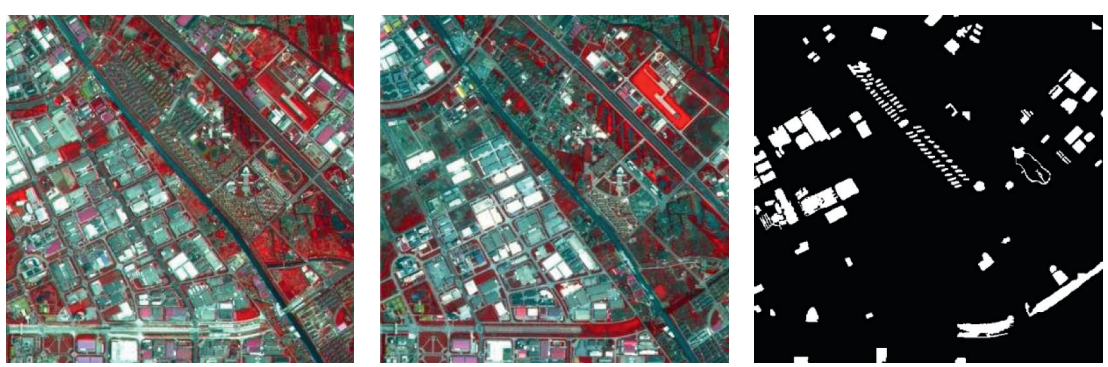

(a) (b) (c)

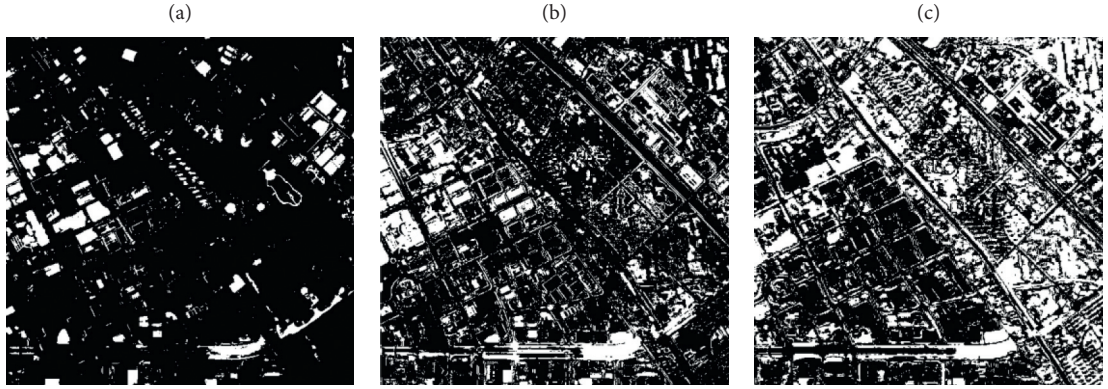

(d) (e) (f)

Figure 5: Continued.

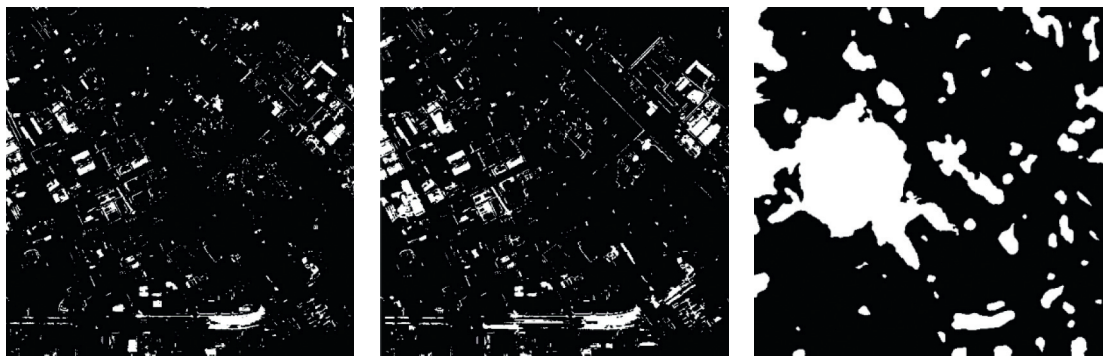

(g) (h) (i)

Figure 5: CD maps of dataset 3: (a-b) dataset 3; (c) reference map of dataset 3; (d–i) CD maps obtained in dataset 3 using the proposed method and Methods 1, 2, 3, 4, and 5, respectively.

Table 4: Quantitative evaluation of CD accuracy in dataset 1.

Method/Indicator Evaluation criteria	OA (%) The higher the better	FP (%) The lower the better	FN (%) The lower the better
Proposed method	83.9	15.1	9.1
Method 1	57.2	40.4	39.1
Method 2	63.5	32.3	25.2
Method 3	79.8	19.3	11.9
Method 4	71.2	28.5	19.4
Method 5	77.1	21.4	15.3

OA, overall accuracy; FP, false positive; FN, false negative.

Table 5: Quantitative evaluation of CD accuracy in dataset 2.

Method/Indicator Evaluation criteria	OA (%) The higher the better	FP (%) The lower the better	FN (%) The lower the better
Proposed method	84.5	12.6	9.8
Method 1	68.4	39.1	34.9
Method 2	72.8	30.6	29.8
Method 3	81.5	15.3	11.4
Method 4	74.8	26.5	24.4
Method 5	51.1	46.6	42.8

Table 6: Quantitative evaluation of CD accuracy in dataset 3.

Method/Indicator Evaluation criteria	OA (%) The higher the better	FP (%) The lower the better	FN (%) The lower the better
Proposed method	85.1	13.9	10.9
Method 1	59.4	40.2	39.7
Method 2	68.6	30.3	31.6
Method 3	78.1	21.9	17.4
Method 4	80.2	19.4	15.8
Method 5	71.4	26.4	27.8

experimental schemes were carried out: (1) manually set the scale parameters of Area, Diagonal, Standard Deviation, and NMI as {100, 918, 1734, 2548, 3368, 4185, 5000}, {10, 25, 40, 55, 70, 85, 100}, {0.2, 0.25, 0.3, 0.35, 0.4, 0.45, 0.5}, and {20, 25, 30, 35, 40, 45, 50} [25], respectively, and the remaining steps were consistent with the proposed method (Method 6); (2) average the extracted CIIs corresponding to pixel i, and traverse all pixels in the image, and make use of EM method [3] to determine a threshold for obtaining the CD map (Method 7). The OA of the different methods are reported in Table 7.

As shown above, the OA of the proposed method was significantly higher than of the other two methods. Therefore, the proposed adaptive scale parameter extraction

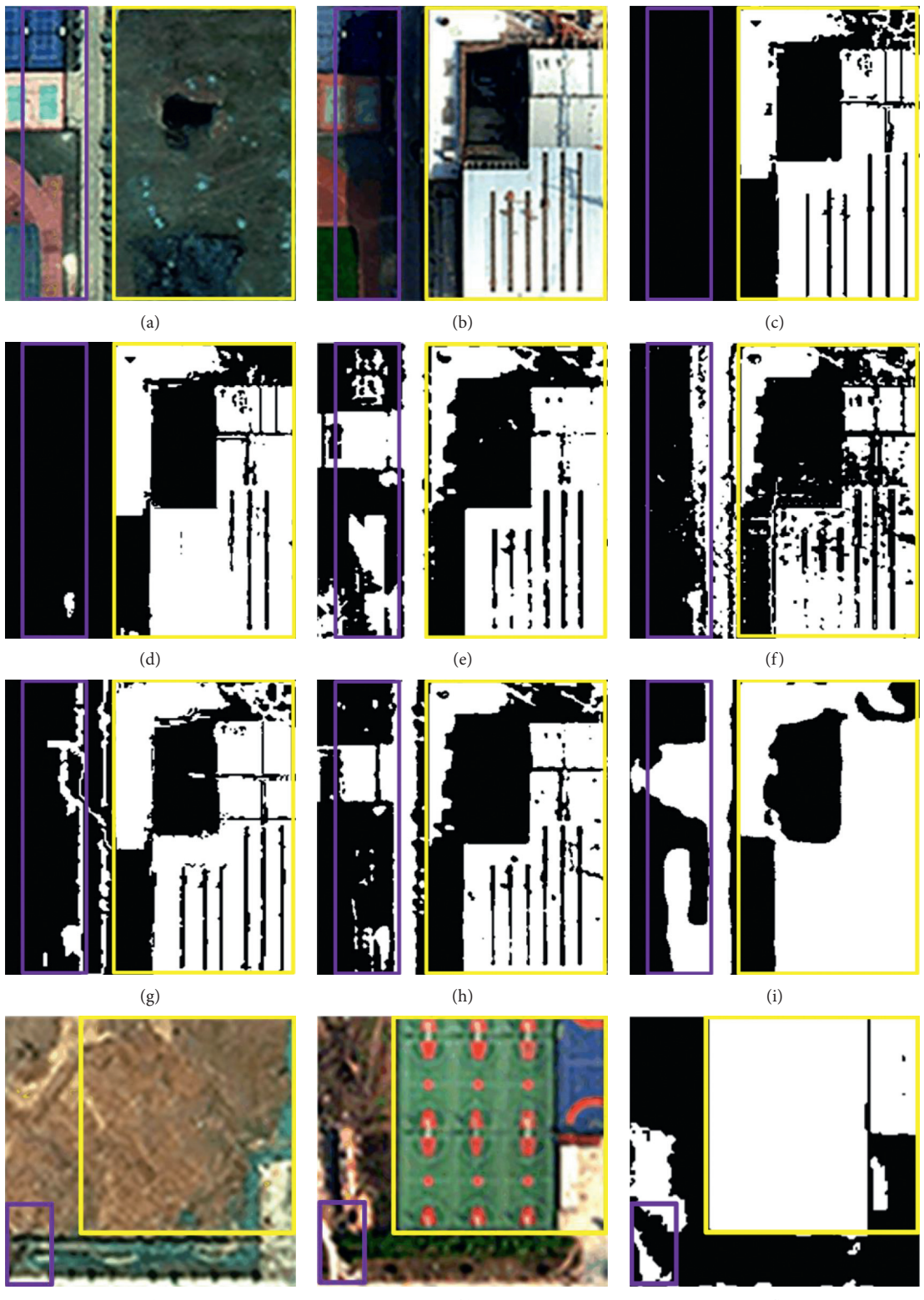

(a) (b) (c)

(d) (e) (f)

(g) (h) (i)

(j) (k) (l)

Figure 6: Continued.

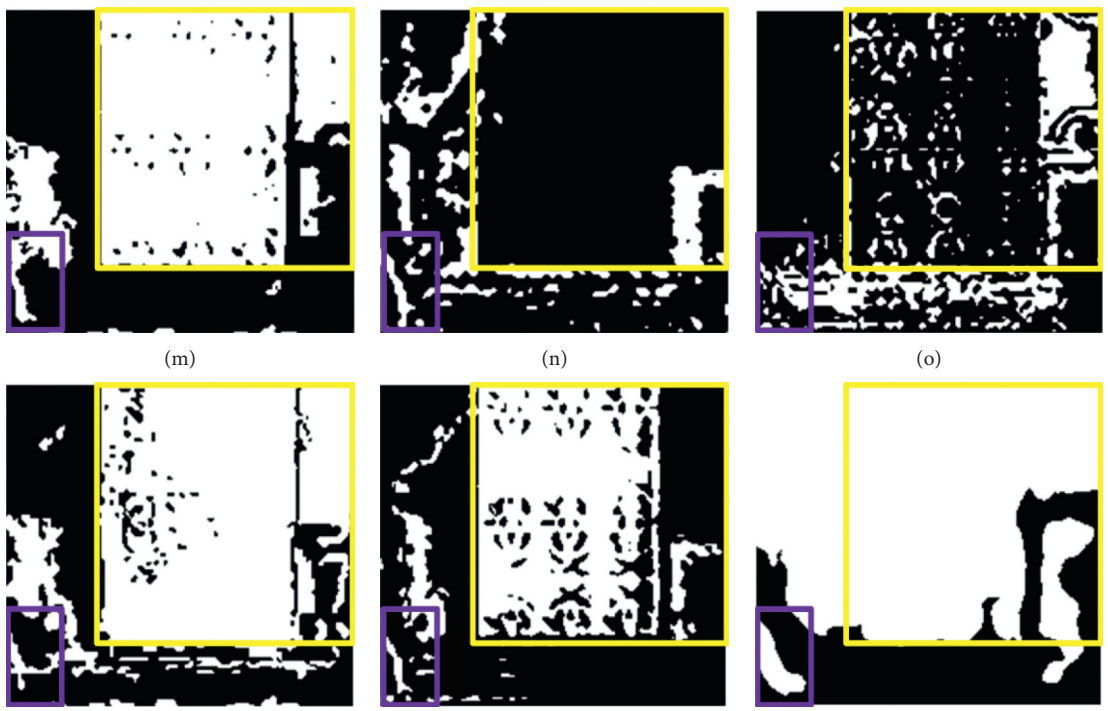

(m) (n) (o)

(p) (q) (r)

Figure 6: CD maps of patches I1 and I2: (a-b) patch I1; (c) reference map of Patch I1; (d–i) CD maps obtained in patch I1 using the proposed method and Methods 1, 2, 3, 4, and 5, respectively; (j-k) patch I2; (l) reference map of patch I2; (m–r) CD maps obtained in patch I2 using the proposed method and Methods 1, 2, 3, 4, and 5, respectively.

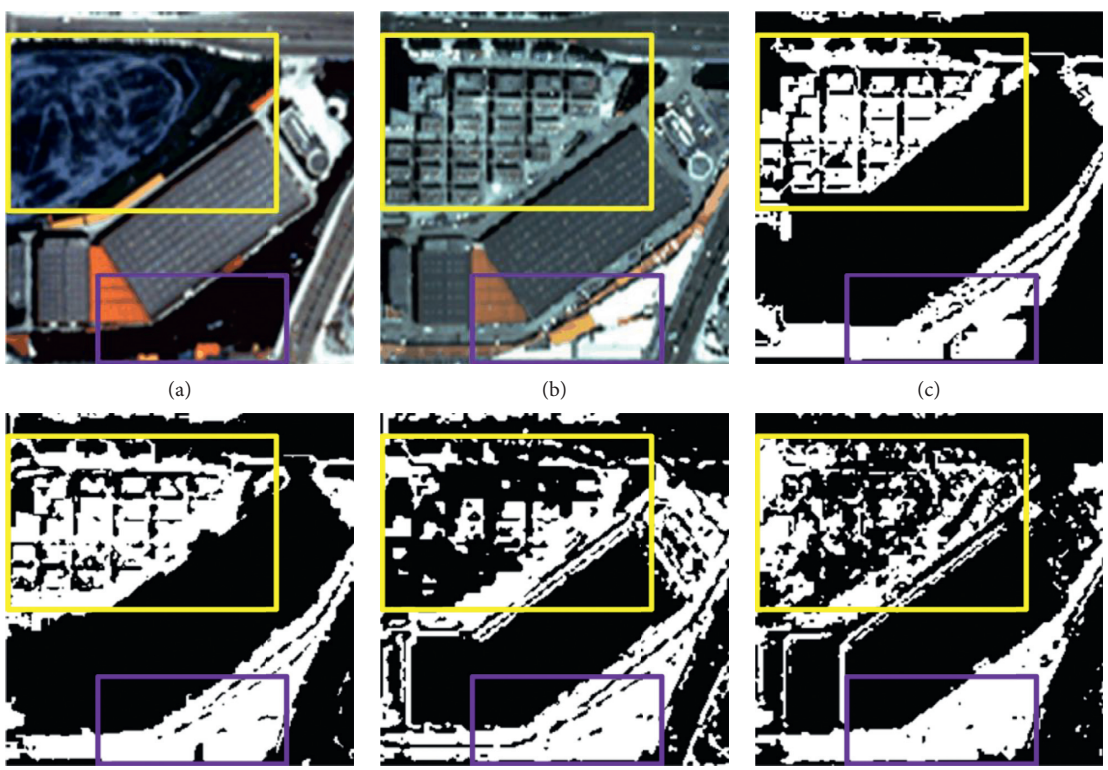

(a) (b) (c)

(d) (e) (f)

Figure 7: Continued.

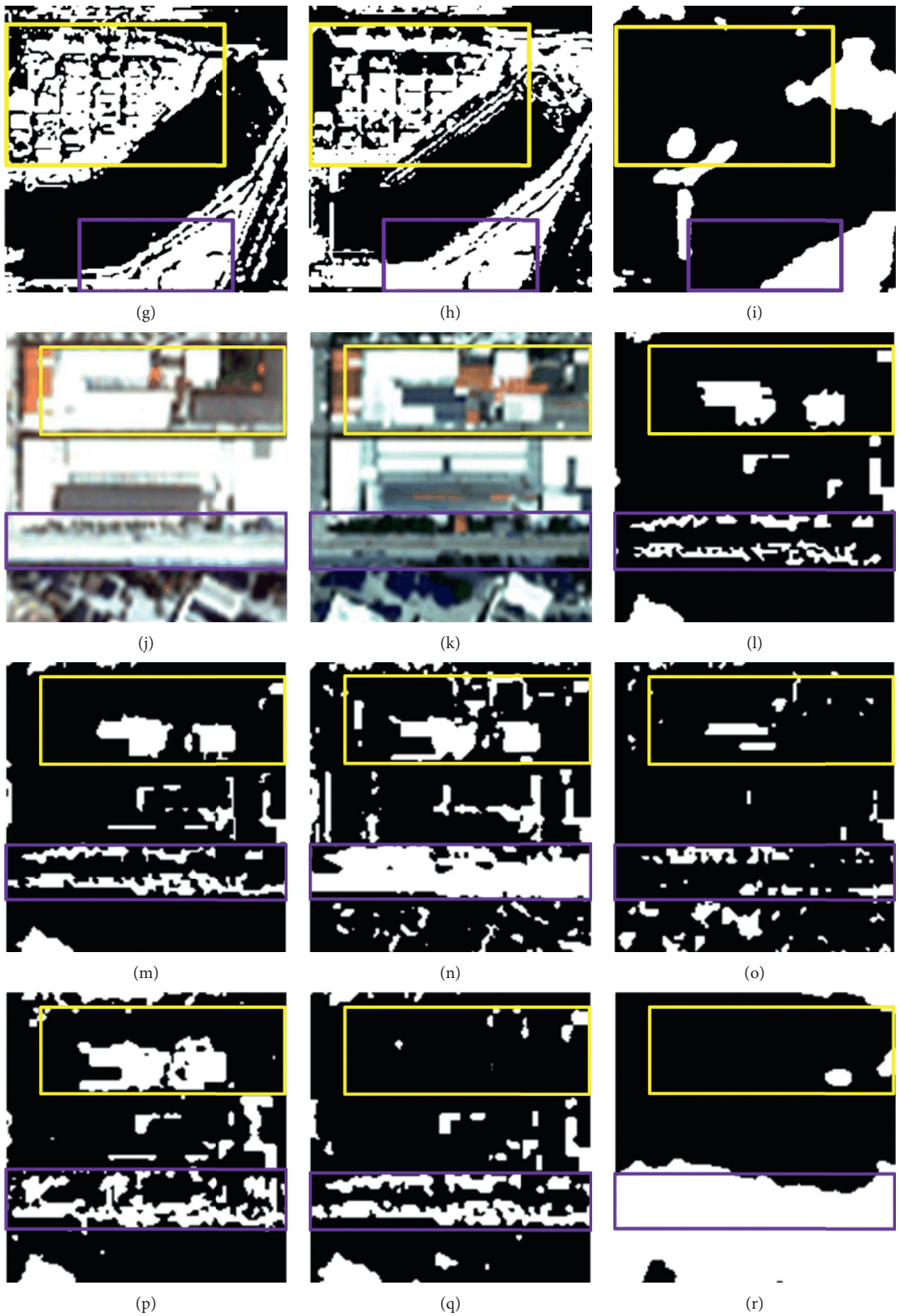

Figure 7: CD maps of patches I3 and I4: (a-b) patch I3; (c) reference map of Patch I3; (d–i) CD maps obtained in patch I3 using the proposed method and Methods 1, 2, 3, 4, and 5, respectively; (j-k) patch I4; (l) reference map of patch I4; (m–r) CD maps obtained in patch I4 using the proposed method and Methods 1, 2, 3, 4, and 5, respectively.

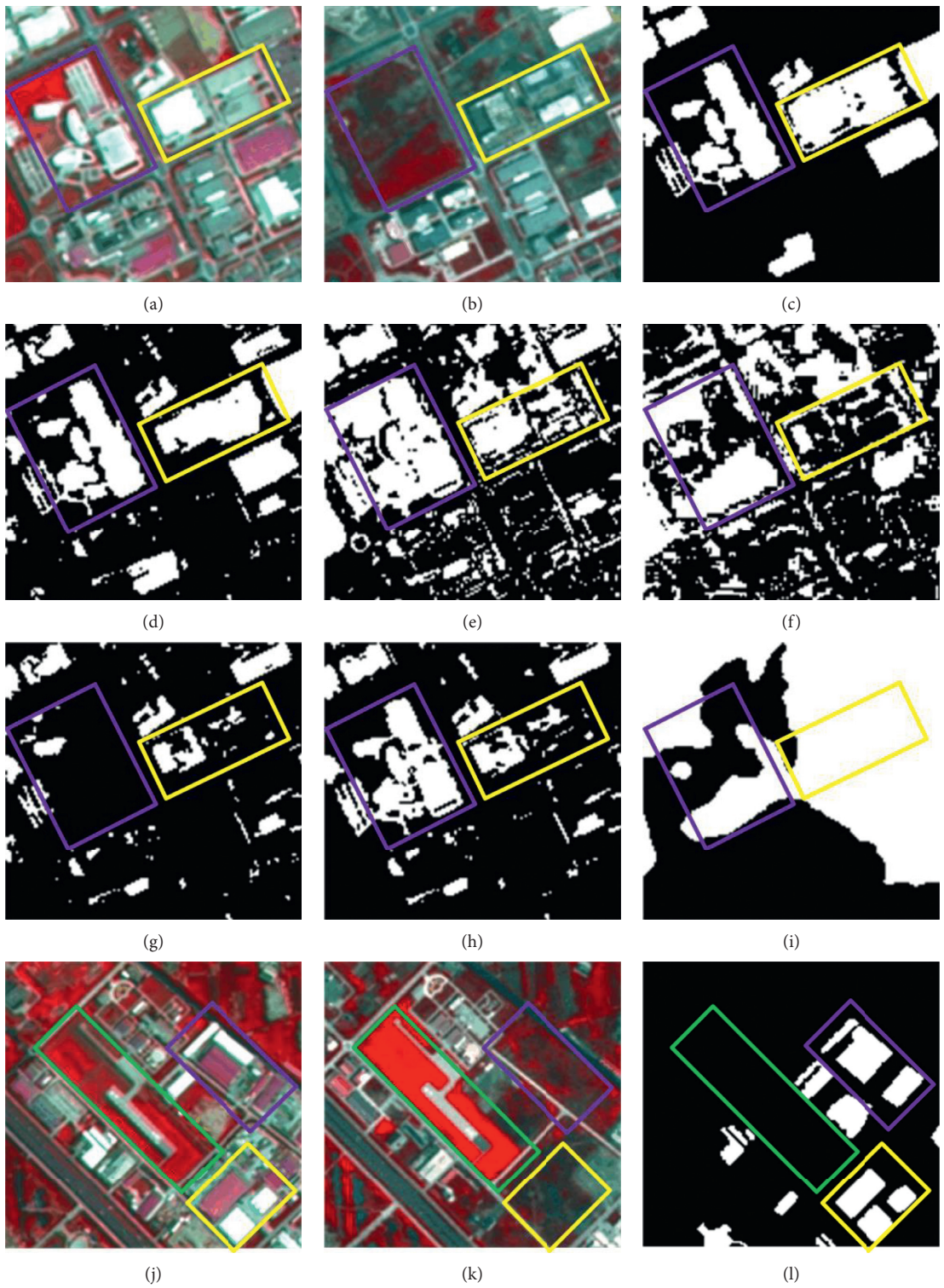

(a) (b) (c)

(d) (e) (f)

(g) (h) (i)

(j) (k) (l)

Figure 8: Continued.

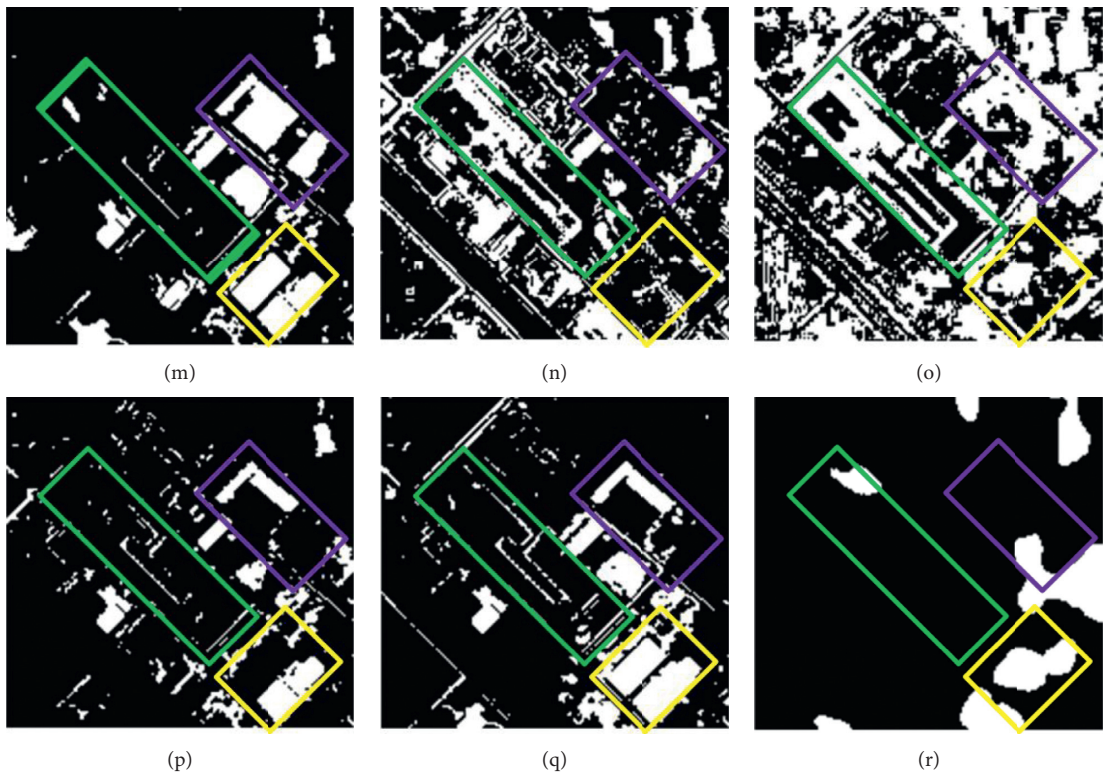

Figure 8: CD maps of patches I5 and I6: (a-b) patch I5; (c) reference map of Patch I5; (d–i) CD maps obtained in patch I5 using the proposed method and Methods 1, 2, 3, 4, and 5, respectively; (j-k) patch I6; (l) reference map of patch I6; (m–r) CD maps obtained in patch I6 using the proposed method and Methods 1, 2, 3, 4, and 5, respectively.

Table 7: OA of the proposed method, Method 6, and Method 7.

Dataset1	Method	Proposed method	Method 6	Method 7
	OA (%)	83.9	76.3	74.1
Dataset 2	Method	Proposed method	Method 6	Method 7
	OA (%)	84.5	72.6	73.8
Dataset 3	Method	Proposed method	Method 6	Method 7
	OA (%)	85.1	74.5	77.3

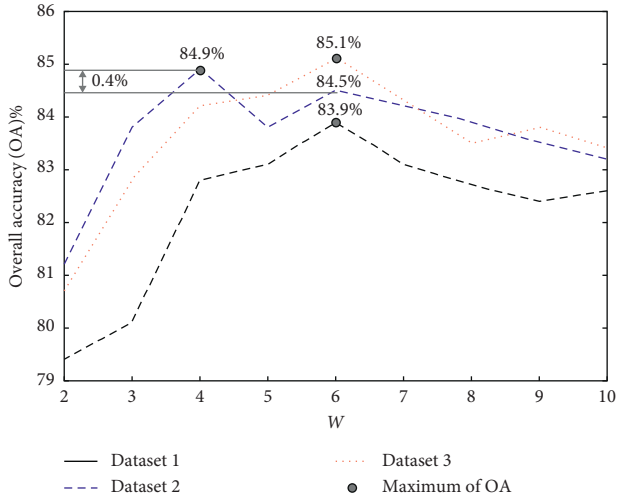

Figure 9: Analysis of the impact on OA with different W.

strategy and decision fusion framework were necessary and effective for improving CD accuracy: the former was helpful to highlight the representative spatial structure information while reducing the reductant information in APs; the latter could improve the reliability of decisions by reducing the uncertainty of change information from different sources.

4.6. Analysis of the Impact on OA with Different W. In the process of adaptive scale parameter extraction, the number of scales, W, was the only the subordinate parameter which should be set manually. In order to specify the setting basis of W, the impact on OA with different W was analyzed in this section. As shown in Figure 9, the horizontal coordinate is W, the longitudinal coordinate is OA, and the results of three datasets are represented by curves in different styles.

As shown above, in the three dataset experiments, with the continuous increase of W, OA shows a similar general

Table 8: Detailed W-OA values in three dataset experiments.

Dataset 1	W	2	3	4	5	6	7	8	9	10
	OA (%)	79.4	80.1	82.8	83.1	83.9	83.1	82.7	82.4	82.6
Dataset 2	W	2	3	4	5	6	7	8	9	10
	OA (%)	81.2	83.8	84.9	83.8	84.5	84.2	83.9	83.5	83.2
Dataset 3	W	2	3	4	5	6	7	8	9	10
	OA (%)	80.7	82.8	84.2	84.4	85.1	84.3	83.5	83.8	83.4

trend of gradual rising at first, then steady, and decreasing in the end. Among them, $W = 6, W = 4$, and $W = 6$ are corresponded to the peaks of OA curves with 83.9%, 84.9%, and 85.1% in the experiments of Datasets 1, 2, and 3, respectively. The detailed values are shown in Table 8.

As shown above, in the experiment of Dataset 2, when W was set as 6, OA could reach 84.5% and was only slightly lower by 0.4% than the corresponding highest OA. This meant the ideal results could be obtained in all experiments of three datasets by setting W as 6. Therefore, considering the automation and reliability, it was suggested to directly set W as 6 in CD applications.

5. Conclusion

In this paper, a novel decision fusion framework based on ASP-MAPs was proposed for CD in HRRS images. By establishing the objective function based on the minimum of average interscale correlation, a set of scale parameters could be adaptively obtained to extract the representative APs while reducing redundant information. On this basis, a multifeature decision fusion framework based on D-S theory was constructed to improve the reliability of decisions by reducing the uncertainty of change information from different sources. The effectiveness of the proposed method was elaborately examined through the experiments on the multitemporal HRRS image datasets. By comparison with five advanced CD methods of different types, the proposed method showed outstanding performance in both quantitative evaluation and visual inspection, and OA reached more than 83.9%, while the fluctuation range was less than 1.5%.

Data Availability

The data used to support the findings of this study are available from the corresponding author upon request.

Conflicts of Interest

The authors declare that they have no conflicts of interest.

Acknowledgments

This work was supported by the Open Research Fund of Jiangxi Province Key Laboratory of Water Information Cooperative Sensing and Intelligent Processing (No. 2016WICSIP004), the Six Talent-peak Project in Jiangsu Province (No. 2019-XYDXX-135), the Jiangsu Overseas Visiting Scholar Program for University Prominent Young and Middle–aged Teachers and Presidents (No. 2018–69), the National Natural Science Foundation of China (No. 61601229), and the Natural Science Foundation of Jiangsu Province (No. BK20160966).

References

[1] J. Sun, "Change detection based on the high-resolution remote sensing images," *Forest Inventory & Planning*, vol. 22, no. 171, pp. 135–144, 2018.

[2] A. Anees and J. Aryal, "Near-real time detection of beetle infestation in pine forests using MODIS data," *IEEE Journal of Selected Topics in Applied Earth Observations and Remote Sensing*, vol. 7, no. 9, pp. 3713–3723, 2014.

[3] L. Bruzzone and D. Prieto, "Automatic analysis of the difference image for unsupervised change detection," *IEEE Transactions on Geoscience and Remote Sensing*, vol. 38, no. 3, pp. 1171–1182, 2000.

[4] A. Anees, J. Aryal, and M. M. O'Reilly, "A robust multi-kernel change detection framework for detecting leaf beetle defoliation using landsat 7 ETM+ data," *ISPRS Journal of Photogrammetry and Remote Sensing*, vol. 122, pp. 167–178, 2016.

[5] G. Liu, Y. Gousseau, and F. Tupin, "A contrario comparison of local descriptors for change detection in very high spatial resolution satellite images of urban areas," *IEEE Transactions on Geoscience and Remote Sensing*, vol. 57, no. 6, pp. 3904–3918, 2019.

[6] S. J. Park, A. R. Achmad, and M. Syifa, "Machine learning application for coastal area change detection in gangwon province, South Korea using high-resolution satellite imagery," *Journal of Coastal Research*, vol. 90, no. 1, pp. 228–235, 2019.

[7] H. Zhuang, K. Deng, and H. Fan, "Strategies combining spectral angle mapper and change vector analysis to unsupervised change detection in multispectral images," *IEEE Geoscience and Remote Sensing Letters*, vol. 13, no. 5, pp. 681–685, 2016.

[8] N. Falco, M. D. Mura, and F. Bovolo, "Change detection in VHR images based on morphological attribute profiles," *IEEE Geoscience and Remote Sensing Letters*, vol. 10, no. 3, pp. 636–640, 2013.

[9] E. M. O. Silveira, F. D. B. Espírito-Santo, and F. W. Acerbi-Júnior, "Reducing the effects of vegetation phenology on change detection in tropical seasonal biomes," *GIScience & Remote Sensing*, vol. 56, no. 5, pp. 699–717, 2019.

[10] W. Ma, H. Yang, and Y. Wu, "Change detection based on multi-grained cascade forest and multi-scale fusion for SAR images," *Remote Sensing*, vol. 11, no. 2, p. 142, 2019.

[11] Y. Zhong, W. Liu, and J. Zhao, "Change detection based on pulse-coupled neural networks and the NMI feature for high spatial resolution remote sensing imagery," *IEEE Geoscience and Remote Sensing Letters*, vol. 12, no. 3, pp. 537–541, 2015.

[12] K. Dickens and A. Armstrong, "Application of machine learning in satellite derived bathymetry and coastline detection," *SMU Data Science Review*, vol. 2, no. 1, 2019.

[13] D. Peng, Y. Zhang, and H. Guan, "End-to-end change detection for high resolution satellite images using improved UNet++," *Remote Sensing*, vol. 11, no. 11, p. 1382, 2019.

[14] Y. Zhang, D. Peng, and X. Huang, "Object-based change detection for VHR images based on multiscale uncertainty analysis," *IEEE Geoscience and Remote Sensing Letters*, vol. 15, no. 1, pp. 13–17, 2018.

[15] Y. Solano-Correa, F. Bovolo, and L. Bruzzone, "An approach for unsupervised change detection in multitemporal VHR images acquired by different multispectral sensors," *Remote Sensing*, vol. 10, no. 4, p. 533, 2018.

[16] Y. Chen and Z. Cao, "An improved MRF-based change detection approach for multitemporal remote sensing imagery," *Signal Processing*, vol. 93, no. 1, pp. 163–175, 2013.

[17] T. Bai, K. Sun, S. Deng, D. Li, W. Li, and Y. Chen, "Multi-scale hierarchical sampling change detection using random forest for high-resolution satellite imagery," *International Journal of Remote Sensing*, vol. 39, no. 21, pp. 7523–7546, 2018.

[18] R. Kishorekumar and P. Deepa, "Automatic change detection using multiindex information map on high-resolution remote sensing images," *Cluster Computing*, vol. 21, no. 1, pp. 39–49, 2018.

[19] P. Shao, W. Shi, and M. Hao, "Indicator-kriging-integrated evidence theory for unsupervised change detection in remotely sensed imagery," *IEEE Journal of Selected Topics in Applied Earth Observations and Remote Sensing*, vol. 11, no. 12, pp. 4649–4663, 2018.

[20] S. Mahdavi, B. Salehi, W. Huang, M. Amani, and B. Brisco, "A PolSAR change detection index based on neighborhood Information for flood mapping," *Remote Sensing*, vol. 11, no. 16, p. 1854, 2019.

[21] M. M. Dalla, J. A. Benediktsson, F. Bovolo, and L. Bruzzone, "An unsupervised technique based on morphological filters for change detection in very high resolution images," *IEEE Geoscience and Remote Sensing Letters*, vol. 5, no. 3, pp. 433–437, 2008.

[22] J. López-Fandiño, D.B. Heras, F. Argüello, and M. Dalla Mura, "GPU framework for change detection in multitemporal hyperspectral images," *International Journal of Parallel Programming*, vol. 47, no. 2, pp. 272–292, 2019.

[23] G. Cavallaro, M. Dalla Mura, J. A. Benediktsson, and L. Bruzzone, "Extended self-dual attribute profiles for the classification of hyperspectral images," *IEEE Geoscience and Remote Sensing Letters*, vol. 12, no. 8, pp. 1690–1694, 2015.

[24] S. Liu, Q. Du, X. Tong, A. Samat, L. Bruzzone, and F. Bovolo, "Multiscale morphological compressed change vector analysis for unsupervised multiple change detection," *IEEE Journal of Selected Topics in Applied Earth Observations and Remote Sensing*, vol. 10, no. 9, pp. 4124–4137, 2017.

[25] M. M. Dalla, B. J. Atli, B. Waske, and L. Bruzzone, "Extended profiles with morphological attribute filters for the analysis of hyperspectral data," *International Journal of Remote Sensing*, vol. 31, pp. 5975–5991, 2010.

[26] H. Luo, C. Liu, C. Wu, and X. Guo, "Urban change detection based on dempster-shafer theory for multitemporal very high-resolution imagery," *Remote Sensing*, vol. 10, no. 7, p. 980, 2018.

[27] B. Chen, J. Wang, and S. Chen, "Prediction of pulsed GTAW penetration status based on BP neural network and D-S evidence theory information fusion," *The International Journal of Advanced Manufacturing Technology*, vol. 48, no. 1–4, pp. 83–94, 2010.

[28] P. Ghamisi, J. A. Benediktsson, and J. R. Sveinsson, "Automatic spectral-spatial classification framework based on attribute profiles and supervised feature extraction," *IEEE Transactions on Geoscience and Remote Sensing*, vol. 52, no. 9, pp. 5771–5782, 2014.

[29] C. Yin, X. Huang, S. Dadras et al., "Design of optimal lighting control strategy based on multi-variable fractional-order extremum seeking method," *Information Sciences*, vol. 465, pp. 38–60, 2018.

[30] C. Yin, S. Wu, S. Zhou, J. Cao, X. Huang, and Y. Cheng, "Design and stability analysis of multivariate extremum seeking with Newton method," *Journal of the Franklin Institute*, vol. 355, no. 4, pp. 1559–1578, 2018.

[31] C.-W. Chow, C.-Y. Chen, and S.-H. Chen, "Enhancement of signal performance in LED visible light communications using mobile phone camera," *IEEE Photonics Journal*, vol. 7, no. 5, pp. 1–7, 2015.

[32] E. Aptoula, M. Dalla Mura, and S. Lefevre, "Vector attribute profiles for hyperspectral image classification," *IEEE Transactions on Geoscience and Remote Sensing*, vol. 54, no. 6, pp. 3208–3220, 2016.

[33] S. L. Hegarat-Mascle, I. Bloch, and D. Vidal-Madjar, "Application of dempster-shafer evidence theory to unsupervised classification in multisource remote sensing," *IEEE Transactions on Geoscience and Remote Sensing*, vol. 35, pp. 1018–1031, 1997.

[34] Y. Shen, C. Wang, and J. L. Hu, "An improved CVA change detection method combining spatial and spectral information," *Remote Sensing Technology and Application*, vol. 34, no. 4, pp. 71–80, 2019.

[35] M. A. Lebedev, Y. V. Vizilter, O. V. Vygolov, V. A. Knyaz, and A. Y. Rubis, "Change detection in remote sensing images using conditional adversarial networks," *ISPRS - International Archives of the Photogrammetry, Remote Sensing and Spatial Information Sciences*, vol. 62, pp. 565–571, 2018.